Electrical Power and Energy Systems 135 (2022) 107341

Contents lists available at ScienceDirect

International Journal of Electrical Power and Energy Systems

journal homepage: www.elsevier.com/locate/ijepes

Development and performance analysis of a multi-functional algorithm for AC microgrids: Simultaneous power sharing, voltage support and islanding detection

Alexandre Serrano-Fontova [a,*], Mohamed Azab [b,c]

[a] Department of Electrical engineering, Technical University of Catalunya (UPC) Barcelona, Spain
[b] EEET Department, Faculty of Engineering, Benha University, Egypt
[c] EEET Department, Yanbu Industrial College, Saudi Arabia

ARTICLE INFO

Keywords:
Microgrids
Distribution networks
Smart grids
Distributed generation

ABSTRACT

A large part of the current microgrids (MGs) operate in grid-connected mode and act as slaves following the voltage and frequency dictated by the main grid. Therefore, these MGs are not expected to be operated in parallel as islands. Hence, according to the IEEE 1457-2018 standard, the power generation units in these grid-connected MGs (GCMGs) have to be disconnected in less than 2 s if islanding occurs. On the contrary, if the islanding operation (IO) does not occur, these MGs exchange power with the electrical grid. This paper explores the feasibility of a multi-functional algorithm (MA) for these GCMGs in an attempt to address three tasks simultaneously; (i) power sharing, (ii) voltage support and, (iii) islanding detection (ID). The MG object of study comprises an electronically interfaced photovoltaic (PV) unit supplemented by a battery energy storage system (BESS) equipped in combination with a bidirectional charger. The model of the GCMG has been implemented in MATLAB, where an extensive set of simulations has been performed. The results demonstrate the effectiveness and benefits of the proposed MA, which fulfils several functions all at once.

1. Introduction

Conceptually, MGs are self-sufficient entities formed by an aggregation of generation units, energy storage systems and a set of controllable loads [1]. These MGs can be either connected to the grid (i.e., the abovementioned GCMGs) or operating in stand-alone mode [2]. Even though these GCMGs can be powered by different technologies (Wind, PV, mini-hydro, etc.), rooftop PV units are becoming very popular in residential and industrial applications due to their multiple benefits. Even though these GCMGs require the main grid, if both generation and storage devices are properly coordinated and sized, the amount of energy exchanged with the grid can be significantly reduced. Therefore, these GCMGs are becoming less grid-dependents in terms of exchanged energy.

In this regard, multi-functional algorithms are gaining momentum in MGs. For example, a fully distributed MA control has been proposed in [3], while references [4–6] used MAs for optimal MG management. If the peak power is shaved and the energy supplied by the grid is curtailed, this will imply a reduction in the electricity cost [7,8]. Undoubtedly, this aspect is crucial for these MGs; for instance, see the techno-economic analysis carried out in [9].

Albeit these MGs offer several advantages for the users and the DNs (e.g., losses reduction and voltage support) [10,11], some issues may occur due to their inherent intermittency. In particular, voltage regulation is among the most concerning issues for the distributor operators (DSOs). Although these PV-based distributed generations (DGs) are commonly operated at unity power factor, some grid codes require reactive power support by the voltage source converters (VSCs). Therefore, optimal Volt/VAR strategies have been investigated for such purposes, see [12]. Presently, the electronically-interfaced grid-connected generation units which provide grid support are also known as grid-following VSCs, see [13].

Abbreviations: BESS, Battery energy storage system; CB, Circuit breaker; DN, Distributed network; DG, Distributed generation; GCMG, Grid-connected Microgrid; ID, Islanding detection; IO, Islanding Operation; LV, Low voltage; LVRT, Low voltage ride through; MA, Multi-functional algorithm; MG, Microgrid; MV, Medium voltage; NDZ, Non-detection zone; PCC, Point of common coupling; PV, Photovoltaic; RE, Renewable energy; ROCOF, Rate-of-change of Frequency; ROCOV, Rate of change of voltage; ROCOVPA, Rate of change of voltage phase angle; SOC, State of charge of batteries; TT, Tripping time; VSC, Voltage source converter.

* Corresponding author.

https://doi.org/10.1016/j.ijepes.2021.107341
Received 7 December 2020; Received in revised form 30 March 2021; Accepted 28 June 2021
Available online 13 September 2021

Moreover, some DSOs have recently established grid codes that oblige the generation units to supply reactive power under steady-state conditions. On the contrary, the reactive-power support during voltage sags is commonly known as low-voltage-ride-through (LVRT) [14]. The BESSs are also used to curtail the injected DG power and prevent grid congestions [15], which is also fostered by the so-called feed-in tariffs [16]. Reference [17] proposes an algorithm to overcome some of the abovementioned drawbacks to increase the PV penetration capacity into the grid through BESSs. The amount of power exchanged between the grid and the MG is reduced and occurs only in scenarios with no PV generation or when the state of charge (SOC) of the BESSs is low. Consequently, the power imbalance between the MG and the main grid is nearly zero on many occasions. Thereby, given this negligible power imbalance, identify the islanding condition becomes a difficult task. Indeed, the most challenging scenarios to detect are those where the power imbalance is close to zero [18].

An IO occurs when a portion of the network that has been isolated from the main grid remains energized. This scenario has been thoroughly analyzed in [18–21,39–42]. A distinction between intentional and unintentional is commonly considered for classifying the islanding scenarios. A major feature of any ID study is the capability of the protective devices to quickly identify the islanding condition [18]. The list of hurdles in case of failure to trip may include PQ disturbances [22] (e.g., frequency and voltage out of range), a safety hazard for the network personnel, or electric machine damaging due to out-of-phase reclosing operations. In this regard, the IEEE Std. 1547 proposes a procedure to follow in these situations and, as mentioned above, suggests a maximum time-disconnection of 2 s [23]. A recent review of the available ID methods and their main characteristics can be found in [24]. The non-detection zone (NDZ) is the most critical indicator in ID studies. It is referred to a specific region defined by active and reactive-power imbalances (i.e., right and left, up and down boundaries) where the ID methods are incapable of identifying the islanding condition.

In general, the advantages of the so-called MAs have been analyzed for many purposes in power systems. In this light, these MAs are used to handle several tasks simultaneously. For example, in Ref. [4], the voltage drops, current unbalances and harmonic distortion compensation tasks are fulfilled all at once. However, some of these algorithms require a real-time communication system between devices, which increase their implementation cost [25]. On the contrary, the MA presented in this paper only uses local measurements of the MG, facilitating its practical implementation. Even though some MAs with multiple input variables have been developed for GCMGs [3], the optimization part of the considered MA only focuses on minimizing the amount of energy interchanged with the grid.

In references [26,27], the ID functionality has been combined with the LVRT capability. Similarly, a multi-task method is presented in [28]. However, the proposed MA goes further within the MGs field, where the power sharing, the voltage support and the ID are coordinated simultaneously.

It is worth noting that, even though the functionalities of the proposed MA have already been addressed separately in recent research studies, a simultaneous evaluation of all issues has not been yet carried out. Crucially, this method has implemented very low thresholds to achieve zero-NDZ during islanding events, which implies a high risk of misidentification during non-islanding events. Nonetheless, the proposed MA has demonstrated high robustness during these events. Additionally, this article also investigates the BESS role for energy storage purposes and as a tool for ID, which has still not been considered in ID studies.

The contribution of the proposed MA lies in the simultaneous combination of the following tasks all at once:

- Power-sharing in the MG.
- Voltage support.
- ID with zero-NDZ.

The rest of the paper is organized as follows; Section 2 details the model of the GCMG and its elements. Section 3 describes the structure and main features of the proposed MA. Section 4 shows and discusses the obtained simulation results. In Section 5, a comparison with other recently published methods is provided. Lastly, Section 6 summarizes the principal conclusions of the paper.

2. Microgrid model

2.1. Test system

The single-line diagram of the implemented three-phase AC model, including the MG and the low voltage (LV) network, is displayed in Fig. 1. The MG is connected to the DN at the 400 V LV grid with a rated frequency of 50 Hz. This LV feeder is connected to the solidly-grounded medium voltage (MV) grid through a 400-kVA delta/wye transformer named TR_3. The short-circuit ratio of the MV infeeder is 150 MVA with an X/R ratio of 7. The LV lines are modelled as series RL impedance. The line impedances and transformers data are summarized in Tables 1 and 2, respectively.

2.2. Data of the photovoltaic unit

The PV unit consists of an aggregate model of PV arrays equipped with a DC/DC buck-boost converter for the maximum power point tracking. The DC/AC conversion is conducted using a three-bridge average-model-based VSC, where the control strategy is shown in Fig. 2(a). In Fig. 2(a), it can be seen that the d-axis component I_d depends on the DC bus voltage error and fed through the proportional-integral (PI_1) regulator. The q-axis component I_q is computed based on the selected reactive power reference Q_1* and fed through PI_2. The two input positions of the bypass switch in Fig. 2(a) allow the user to either enable grid voltage support or provide only the reactive-power required by the MG loads (MGLs). The VSC of the PV unit (i.e., the one represented by VSC_1 in Fig. 1) is connected to the PCC through a filter, a step-up transformer named TR_1, plus the line impedance Z_{L4}. Table 3 presents the data of the PV unit and the VSC_1.

2.3. Battery energy storage system

The implemented BESS is based on a 400 V-390 Ah Lithium-Ion battery. The details of the implemented model of the battery can be found in the power systems toolbox of MATLAB [29]. The charging and discharging control of the battery is carried out through a bidirectional charger based on a three-bridge average-model-based named VSC_2, see Fig. 2 (b). The d-axis component I_d is computed based on the selected reference P_1* and is fed through PI_3. The first position of the bypass switch enables the controller to increase the injected active-power to reduce both the voltage drop and grid losses along with the DN. In contrast, the second position set the charger's active-power reference based on the difference between PV generation and MGLs.

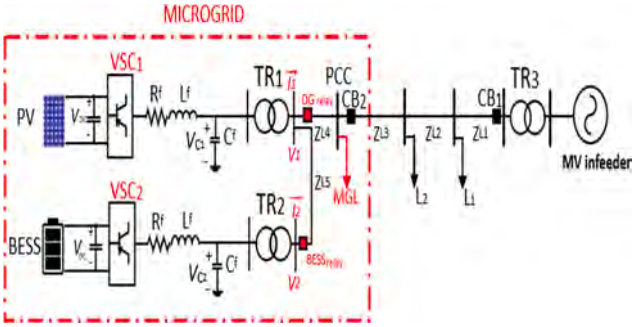

Fig. 1. Single-line diagram of the system under study.

Table 1
Benchmark LV grid data.

Line	Z_1 (Ω/km)	Z_0 (Ω/km)	Distance (km)	Cross-section (mm^2)
L1	0.15 + j0.143	0.62 + j0.572	0.35	150
L2	0.3 + j0.144	1.2 + j0.57	0.25	120
L2	0.3 + j0.144	1.2 + j0.57	0.25	120
L4	0.3 + j0.144	1.2 + j0.57	0.15	120
L5	0.66 + j0.15	2.4 + j0.62	0.2	35

Table 2
Transformer data.

Transformer designation	Power (MVA)	ε (%)	Voltage ratio	Windings Connection
TR1	0.15	4	260/400 V	Wye/Delta
TR2	0.1	3.8	260/400 V	Wye/Delta
TR3	0.4	4.5	25/0.4 kV	Delta/Wye

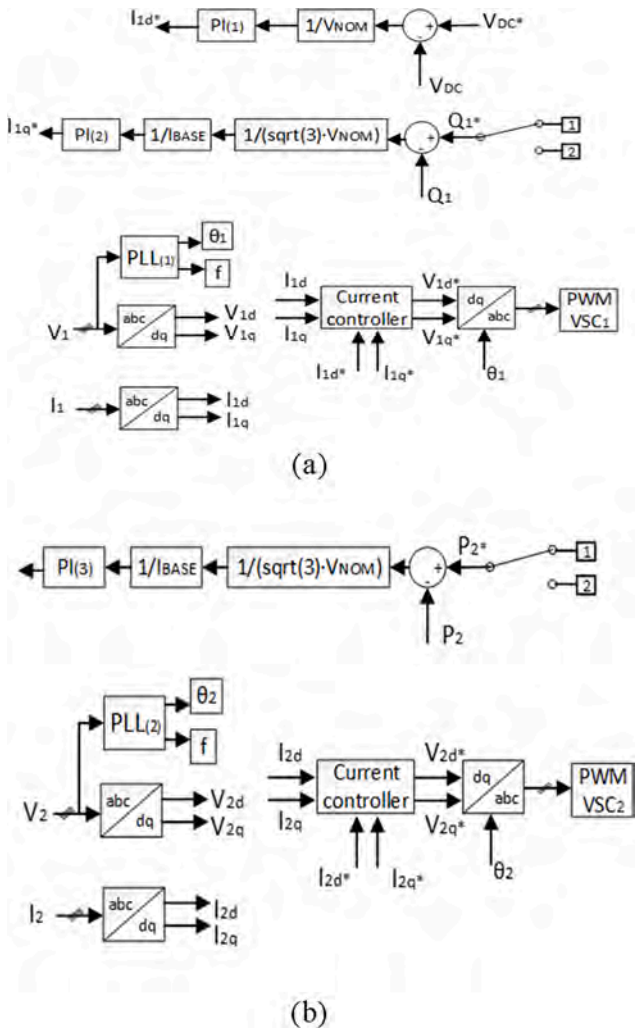

Fig. 2. Control strategies of the two VSCs of the MG. (a) VSC_1. (b) VSC_2.

The q-axis component I_q is set to zero, and therefore the BESS operates at unity power factor. As shown in Fig. 2(b), the VSC_2 is connected to the secondary winding of the TR_1 through the filter, the step-up transformer named TR_2, plus the line impedance Z_{L5}. The main features of the BESS unit and the VSC_2 are provided in Table 4.

Table 3
PV and VSC_1 Features.

Element	Description
PV Array (Model SPR-305E)	Parallel strings (m): 66 Series-connected per string (n): 5 V_{oc} = 64.2 V; I_{sc} = 5.96 A P_{DG} = 100 kW (rated PV power) V_{DC} = 500 V (rated DC link voltage)
VSC_1 (controller features)	PI $_{(1)}$ [Kp = 7; Ki = 800] PI $_{(2)}$ [Kp = 10; Ki = 15300] Current regulator gains [Kp = 0.3; Ki = 20] f_s = 10 kHz (Switching frequency) R_f = 2 mΩ; L_f = 6 mH (RL filter); C_f = 2 μF; C_{DC} = 0.1mF V_{AC} = 260 V (rated AC phase-to-phase voltage) S_{VSC_1} = 100 kVA K_1 = 2.5; K_2 = 5; (Droop gains)

Table 4
BESS and VSC_2 Features.

Element	Description
Lithium-Ion Battery	V = 400 V; Rated capacity = 390 Ah $P_{MAX\_BATT.}$ = 50 kW (instantaneous power) Battery response time = 0.2 s Internal resistance = 7 mΩ
VSC_2 (controller features)	PI $_{(3)}$ [Kp = 10; Ki = 15300] Current regulator gains [Kp = 0.3; Ki = 20] f_s = 10 kHz (Switching frequency) R_f = 2 mΩ; L_f = 6 mH (RL filter); C_f = 2 μf; C_{DC} = 1 mF V_{AC} = 260 V (rated AC phase-to-phase voltage) S_{VSC_2} = 60 kVA Q_{VSC} = 0 kVAr. K_3 = 1.5; (Droop gain)

2.4. Details of the voltage source converters

Presently, synchronous controllers are widely utilized in power converter applications. The initial time-variant variables are transformed into time-invariant, so the linear control is achieved without introducing steady-state error [30]. Thus, to control the VSCs in the MG, the three-phase measurements in the abc reference frame are firstly transformed into the two-axis dq reference frame. Fig. 2 illustrate the process with the implemented abc-to-dq blocks. By decoupling the direct and quadrature components, the regulation of active and reactive powers is achieved separately, see [31].

Both inner and outer loops carry out the control of each VSC. In VSC_1, there are two outer loops according to both the DC bus voltage and reactive-power errors and one inner loop for the current control. On the other hand, in VSC_2, the outer loop controls the active-power, while the inner loop belongs to the current control. The details of these controllers are provided in Tables 3 and 4, respectively. A comprehensive survey of power converters and how to tune these controllers can be found in [32].

3. Description of the proposed multi-functional algorithm

3.1. Algorithm structure

The description of this MA is illustrated in Fig. 3, and the details are provided below. However, in order to provide a clear understanding of the MA, the flowchart explanation has been divided into several stages as follows.

The first stage of the algorithm focuses on data mining, which involves two tasks (see the first two blocks of the flowchart in Fig. 3). The first task is to obtain the voltage measurements at the PCC, and the second on computing the state variables required for the ID process. Hence, the time-domain vector of the computed state variables is defined as follows:

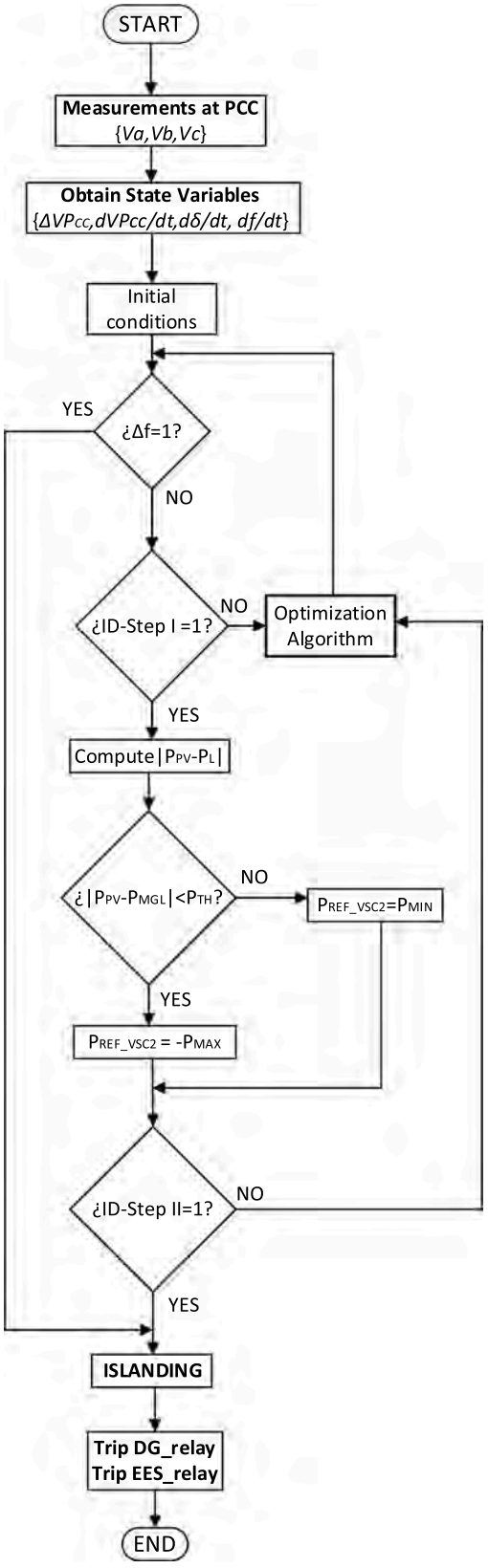

Fig. 3. Flowchart of the proposed MA.

$$[X^j_{1,k}(t)]^T = [x^j_{1,k}(t_1), x^j_{1,k}(t_2), x^j_{1,k}(t_3), \cdots, x^j_{1,k}(t_n)] \tag{1a}$$

$$[X^j_{2,k}(t)]^T = [x^j_{2,k}(t_1), x^j_{2,k}(t_2), x^j_{2,k}(t_3), \cdots, x^j_{2,k}(t_n)] \tag{1b}$$

$$[X^j_{3,k}(t)]^T = [x^j_{3,k}(t_1), x^j_{3,k}(t_2), x^j_{3,k}(t_3), \cdots, x^j_{3,k}(t_n)] \tag{1c}$$

$$[X^j_{4,k}(t)]^T = [x^j_{4,k}(t_1), x^j_{4,k}(t_2), x^j_{4,k}(t_3), \cdots, x^j_{4,k}(t_n)] \tag{1d}$$

where $X^j_{m,k}(t)$ is the mth state vector for a particular jth event at the kth target location. These vectors can also be expressed using the following transposed 4-dimension vector expression:

$$X^j_{m,k}(t)^T = \begin{bmatrix} X^j_{1,k}(t_i) \\ X^j_{2,k}(t_i) \\ X^j_{3,k}(t_i) \\ X^j_{4,k}(t_i) \end{bmatrix}; X^j_{m,k}(t_i) \in M_{1x4} \tag{2}$$

As mentioned earlier, this vector captures the time-domain variables during the desired period t_n. The state variables for every jth event at every kth location are defined in Table 5. Considering N events, the matrix expression of the whole range of events can be expressed as an $N \times 4$ matrix:

$$X_k(t_i) = \begin{bmatrix} x^1_{1,k}(t_i) & \cdots & x^1_{4,k}(t_i) \\ \vdots & \ddots & \vdots \\ x^N_{1,k}(t_i) & \cdots & x^N_{4,k}(t_i) \end{bmatrix}; X_k(t_i) \in M_{Nx4} \tag{3}$$

The state vector X_k expressed in (3) is obtained from the three-phase voltages measurements at the PCC.

The second stage of this algorithm begins with the first decision block (DB) in Fig. 3, which contains the frequency protection. This protection has been set to 49 Hz and 51 Hz for both under and over-frequency. If the output of this DB is true, the islanding condition has already been identified. On the contrary, if this output is false, the second DB of Fig. 3 checks the state of the ID-STEP1 (see the logic-gate diagram in Fig. 4). As can be seen in Fig. 4, this DB outputs a true value in case the following constraints are accomplished; voltage remains between 0.9 pu and 1.1 pu, the absolute value of the voltage derivative $|dV_{PCC}/dt|$ is below 0.1 pu/s for 150 ms and the $|d\delta/dt|$ is above 1 deg./s for at least 250 ms. If this second DB outputs a true signal, the power imbalance between PV generation and MGLs is computed. If not, the optimization algorithm block is initiated. For the sake of clarity, the main features of the optimization algorithm sub-block are provided separately in the following subsection, whilst its flowchart is displayed in Fig. 5.

The third stage is targeted at setting the optimal active-power reference for the battery charger required to force the ROCOVPA to be non-zero, carried out through the third DB of the flowchart illustrated in Fig. 3. In this respect, if the absolute value of the active-power imbalance is below a particular established threshold P_{TH}, the charger reference value is assigned to its maximum charging value (i.e., $-P_{MAX}$). On the other hand, if this value exceeds this $P_{TH,}$ the charger reference is set to P_{MIN} (i.e., 0 kW). In this case, P_{TH} is set to 10 kW. Note that a positive sign for active power indicates discharging mode, whereas a negative

Table 5
State Variables.

Symbol	Variable	
x_1	V_{PCC}	Voltage at PCC in (pu)
x_2	dV_{PCC}/dt	ROCOV (pu/s)
x_3	$d\delta/dt$	ROCOVPA (deg./s)
x_4	df/dt	ROCOF (deg./s)

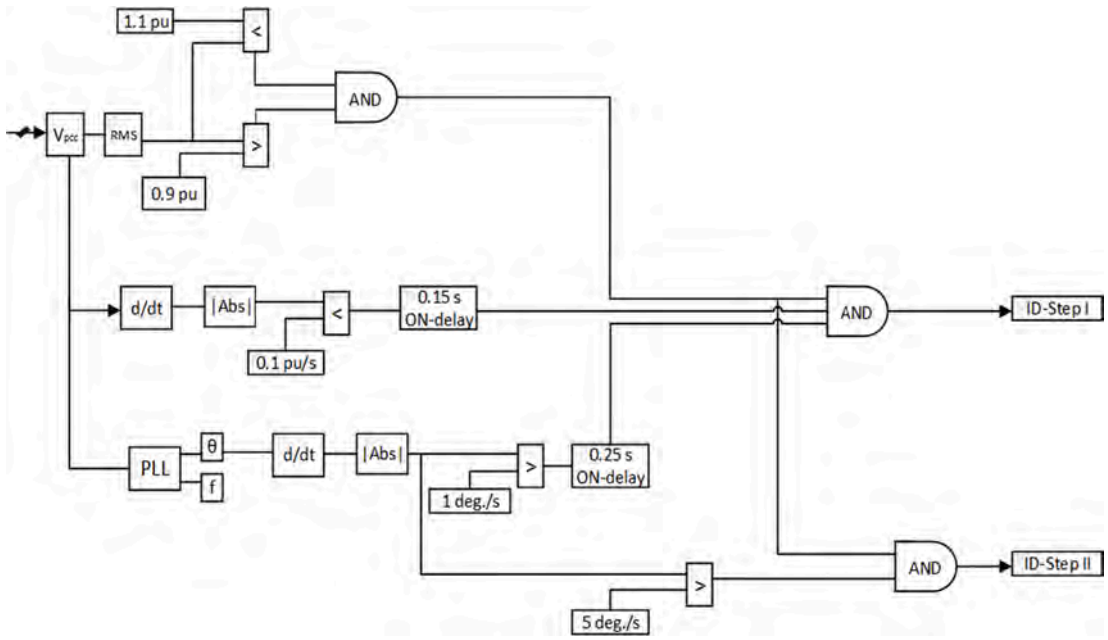

Fig. 4. Logic gate diagram of the implemented passive-based ID steps of the MA.

one means charging mode.

The fourth stage is the last part of the algorithm, which will determine whether the event is, in fact, an IO. In this vein, the fourth DB supervises if following the ID-STEP 2 outputs a true value after the battery charger reference change. That is, if the $|d\delta/dt|$ is above 5 deg./s (see the logic gate diagram displayed in Fig. 4). In case the output of this DB is true, the islanding condition has been identified, and the CB tripping of both PV and BESS relays is ordered. Otherwise, the optimization algorithm is initiated.

3.2. Active and reactive power reference generation

As seen in the previous section, if the output of either DB 2 or 4 of the flowchart in Fig. 3 is false, the optimization block of Fig. 3 sets the reference for both active and reactive powers in each VSC. The power references of this sub-block are dictated by the voltage at the PCC according to the flowchart displayed in Fig. 5. As it only operates between 0.9 and 1.1 pu, no reactive power is injected during grid faults. Therefore, this means that the LVRT has not been considered in this paper.

Thus, the equations required for obtaining both active and reactive power references in each VSC are defined hereunder. Firstly, the control of VSC_1 is analyzed. The active-power delivered by the VSC_1 depends on the maximum power of the PV available at any time instant. This power can be computed as follows

$$P_{MPP}(t_i) = (nV_{MPP})\cdot(I_{MPP}(t_i)m) \tag{4}$$

where $P_{MPP}\ (t_i)$ is the maximum power point (MPP) value of the PV at any time instant, V_{MPP} is the MPP voltage value, and $I_{MPP}\ (t_i)$ is the current corresponding to the MPP of the PV cell at any time instant, n and m are the series-connected modules per string and the parallel strings respectively. The term $I_{MPP}\ (t_i)$ also depends on the temperature and the solar irradiation, see [8].

On the other hand, the reactive-power reference is defined by the following piecewise function:

$$Q_{ref\_VSC1}\ (t_i) = \begin{cases} -Q_{MAX}\ (t_i) & V^{pu}_{PCC}(t_i)\geqslant 1.03 \\ Q_{MGLs}(t_i) + Q_{reg\_1}(t_i) & 1.03 > V^{pu}_{PCC}(t_i)\geqslant 0.95 \\ Q_{MGLs}(t_i) + Q_{reg\_2}(t_i) & 0.95 > V^{pu}_{PCC}(t_i)\geqslant 0.93 \\ Q_{MAX}(t_i) & V^{pu}_{PCC}(t_i) < 0.93 \end{cases} \tag{5}$$

where Q_{MAX} is the maximum reactive-power delivered by the inverter expressed in kVAr, V_{PCC} is the RMS value of the phase voltage at the PCC in pu at any time instant t_i, Q_{reg_1} and Q_{reg_2} are the reactive-power regulators required to carry out the voltage support, if such option is selected (see the bypass switch in Fig. 2(a)). Note that a positive sign for the reactive power in VSC_1 indicates capacitive mode, whereas negative means inductive mode. These droop-based reactive-power regulators are computed as in

$$Q_{reg\_1}(t_i) = ((1 - V^{pu}_{PCC}(t_i))K_1)\cdot|Q_{MAX}(t_i)| \tag{6}$$

$$Q_{reg\_2}(t_i) = ((1 - V^{pu}_{PCC}(t_i))\,K_2)\cdot|Q_{MAX}(t_i)| \tag{7}$$

where K_1 and K_2 are the droop gains of each reactive-power regulator. The maximum reactive-power injected by the VSC_1 at any time instant $Q_{MAX}(t_i)$ can be computed as in:

$$Q_{MAX}(t_i) = \sqrt{S^2_{VSC\_1} - P_{pv}(t_i)^2} \tag{8}$$

where S_{VSC_1} is the rated apparent power of the VSC_1 (see details in Table 3).

Secondly, the active-power reference adjusted in the VSC_2 at any time instant t_i is given by the following model:

$$P_{ref\_VSC2}(t_i) = \begin{cases} P_{pv}(t_i) - P_{MGL}(t_i) & V^{pu}_{PCC}(t_i)\geqslant 0.93 \\ (P_{pv}(t_i) - P_{MGL}(t_i)) + P_{reg} & otherwise \end{cases} \tag{9}$$

where the term P_{MGL} represents the MG loads and P_{reg} denotes the additional amount of active-power provided by the charger for voltage drop minimization if such option is enabled (see the bypass switch in Fig. 2(b)).

The total amount of MG loads is modelled as a balanced three-phase composite load model. An explanation of the voltage-dependent load model considered in this paper can be found in [20]. The term P_{MGL} can be computed as follows:

$$P_{MGL}(t_i) = \sum P_{cnt.z}(t_i) + P_{cnt.I}(t_i) + P_{cnt.P}(t_i) \tag{10}$$

The term P_{reg} included in (9) is obtained through the following droop-based equation:

$$P_{reg}(t_i) = ((1 - V^{pu}_{PCC})\,K_3)\cdot P_{MAX}(t_i) \tag{11}$$

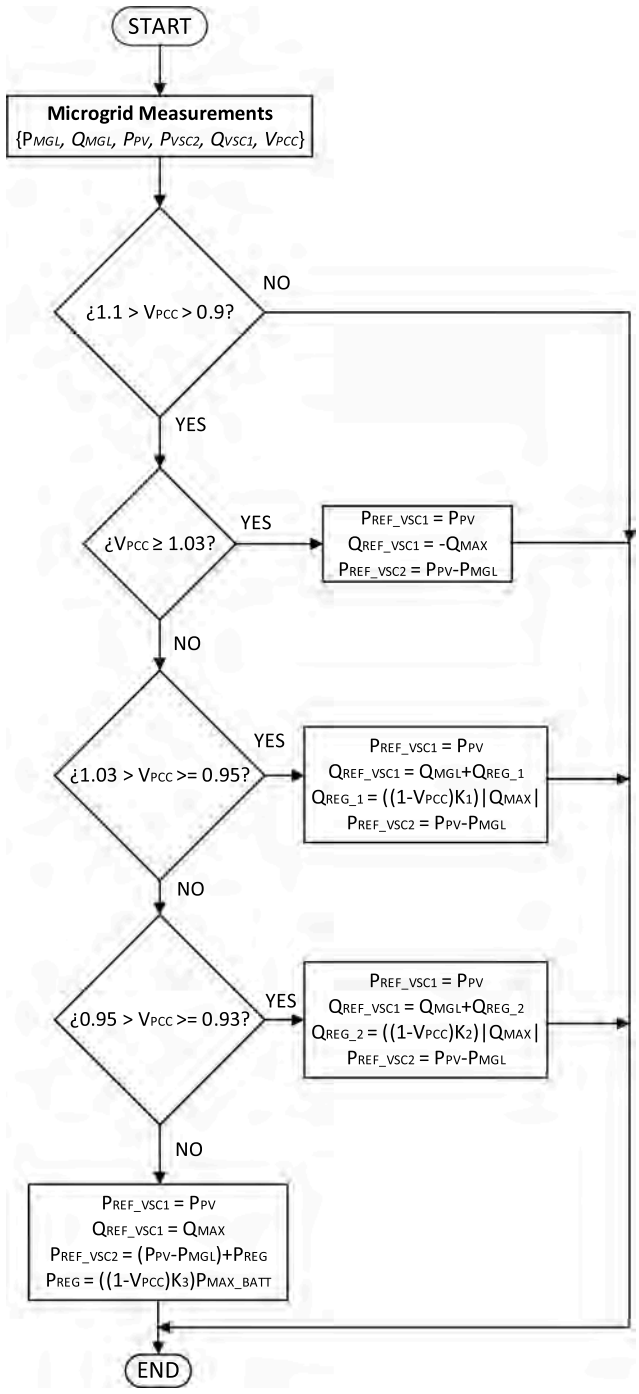

Fig. 5. Flowchart of the optimization algorithm sub-block.

where K_3 is the droop gain and P_{MAX} is the maximum power delivered by the battery charger. Since the VSC_2 has been designed to operate at a unity power factor, the maximum active-power provided by the battery has to be lower or equal to its apparent-power. Thus, the following constraint has to be accomplished:

$$P_{MAX}(t_i) \leqslant S_{VSC\_2} \tag{12}$$

4. Simulation results

4.1. Introduction

This section summarizes the study carried out to assess the effectiveness of the proposed MA in the test system described in Section 2. In this regard, two sets of simulations have been carried out. The first one is aimed at evaluating the optimization algorithm, and therefore it is assumed that any IO occurs during these events.

In order to evaluate the ID capabilities, the second group of simulations have considered the occurrence of islanding scenarios with a wide range of power imbalances. In Section 4.4, a sensitivity analysis of the selected thresholds for the ID is provided. Additionally, to test the reliability of the ID functionality of the MA, a set of non-islanding events has also been simulated.

Eventually, an in-depth discussion about the obtained results of both sets of simulations is provided in the last part of this section.

4.2. Power sharing and voltage support capabilities

As is deduced from the flowchart in Fig. 3, the optimization block is initiated if any islanding condition is suspected. Thereby, the main objective of this block focuses on testing the capabilities of both VSCs in terms of power-sharing and voltage support for various MG load profiles.

Considering the above, four case studies have been simulated for a 24-hour time framework. These simulations have been performed considering a discrete solver with a 50 μs time step over a 48 s simulation time. Each second in the simulation represents a 30-minute in real-time. Thus, the changes in both the PV irradiance and load profiles take place in a 2-second interval. The simulations have been performed in MATLAB [29], taking advantage of a 2.3 GHz intel i7-10510 processor, where each 48-s simulated scenario time took 58 min in real-time. The irradiance profile of the PV unit has been selected from a typical 24-hour pattern [35].

The first case study has considered a particular load profile for both the MG and LV feeder loads. The voltage support capability is enabled in this case, implying that the voltage at the PCC dictates the reactive-power reference of VSC_1.

The second case is based on the same load and PV profiles used in the first case. However, the voltage support for both VSCs is disabled, and the reactive-power reference is dictated by the amount of reactive power drawn by MGLs.

The third case considers an increase in the load profile for both the MG and LV feeder loads named L_1 and L_2 (see the load buses in Fig. 1). This load increase causes larger voltage drops at the PCC with respect to the previous two case studies. Voltage support is enabled in this case.

The fourth case has simulated the same load profile as in the third case, but the voltage support is disabled. Essentially, the purpose of cases 3 and 4 is to observe the increase in both active and reactive powers provided by the two VSCs, according to Eqs. (5) and (11).

The results of these four cases are displayed in the double-column Fig. 6. The left-hand column of Fig. 6 illustrates the results obtained in the first two case studies, whereas the right-column show the ones obtained in the third and fourth case studies, respectively. In each column of Fig. 6, four plots are shown, which from top to bottom are the following; the PCC voltage, the active and reactive powers supplied by the VSC_1, the active power delivered by VSC_2, and the powers measured at the PCC.

The results of the case studies where the voltage support is enabled are displayed in blue (i.e., cases 1 and 3), while the results of the cases where the voltage support is disabled are shown in black (i.e., cases 2 and 4). Since the only difference between cases 1 and 2 and cases 3 and 4 is the reactive-power, the active-power is displayed in green for all plots of Fig. 6.

The effects of the additionally supplied reactive-power are observed in the first plot of Fig. 6. This contribution is particularly noticeable between cases 3 and 4 (see the first plot of the second column of Fig. 6), where the LV feeder's load profile has been increased. Thus, in the right-hand column of Fig. 6, it is observed that the reactive power of VSC_1 reaches its maximum value between t = 4 s and t = 20 s and decreases as

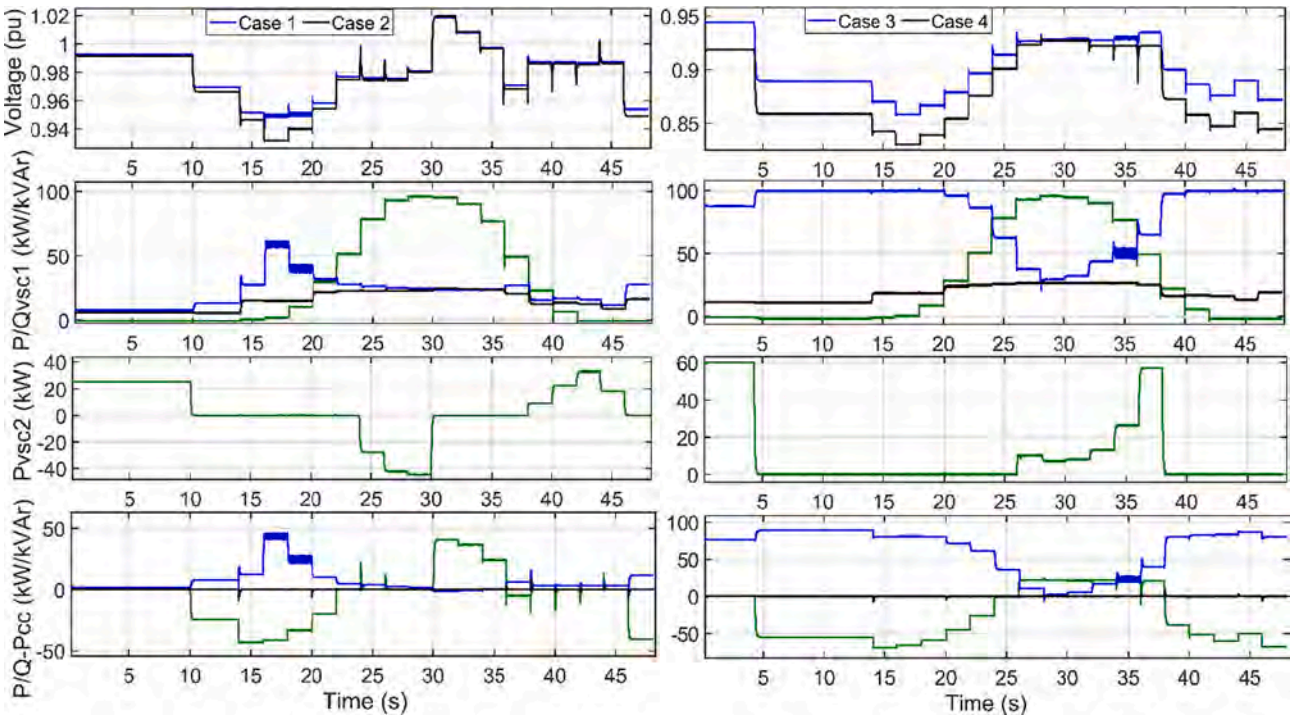

Fig. 6. Results of the four simulated case studies of Section 4.2.

the active power delivered by the PV increases according to (8). This reduction in the reactive power can be observed between t = 20 s and t = 38 s (i.e., between 10 am and 7 pm in the real-time daily hour) due to the active-power injected by the PV unit.

Although the algorithm mainly aims at reducing the energy exchanged with the grid for both positive and negative power imbalances, this cannot be fulfilled if the battery reaches the established SOC constraints. Since these scenarios have not been simulated in real-time, these constraints are implemented by setting the battery charger reference to zero during these periods.

Considering that the second part of the ID functionality takes advantage of the charging strategy, upper and lower SOC limits must be established to endow enough active power. Purposefully, the SOC constraints in the BESS (both above and under) have been set to 90% and 10%, respectively. These SOC capacity constraints are observed in the four case studies. For example, between t = 10 s and t = 24 s in case studies 1 and 2, or between t = 30 s and t = 38 s in case studies 3 and 4, respectively (i.e., between 5 am and 12 am, or between 3 pm and 7 pm in the real-time daily hour).

4.3. Islanding detection functionality

The reliability of the ID functionality implemented in the proposed MA is detailed in this section. The discussion of the results has been

Table 6
Islanding Events description.

Trained case	Voltage support * (E/D)	ΔP* (%)	ΔQ* (%)	ΔP_{PCC}* (%)	ΔQ_{PCC}* (%)	Load composition* (% Cnt Z, % Cnt I, % Cnt P)	Event description	TT* (ms)
1	D	−0.17	−0.2	≈ 0	≈ 0	(73%,0%,27%)	CB 2 opening	526
2	E	−0.17	−8.2	≈ 0	−8.2	(73%,0%,27%)	CB 2 opening	111
3	D	−14	−0.1	≈ 0	≈ 0	(36%,0%,64%)	CB 2 opening	475
4	E	−14	−8	≈ 0	−8	(36%,0%,64%)	CB 2 opening	119
5	D	14	−0.2	≈ 0	≈ 0	(73%,0%,27%)	CB 2 opening	688
6	E	14	−8.1	≈ 0	−8.1	(63%,0%,27%)	CB 2 opening	115
7	D	34	−0.2	≈ 0	≈ 0	(63%,0%,37%)	CB 2 opening	550
8	E	34	−8.2	≈ 0	−8.2	(63%,0%,37%)	CB 2 opening	111
9	D	14	−0.2	14	−0.2	(63%,10%,27%)	CB 2 opening	115
10	E	14	−8.1	14	−8.1	(63%,10%,27%)	CB 2 opening	112
11	D	34	−0.2	34	−0.2	(63%,20%,17%)	CB 2 opening	211
12	E	34	−5.2	34	−5.2	(63%,20%,17%)	CB 2 opening	208
13	E	≈ 0	≈ 0	31.8	−8.2	(89%,0%,11%)	CB 1 opening	213
14	E	15.9	≈ 0	31.8	−8.2	(75%,10%,15%)	CB 1 opening	113
15	E	≈ 0	12.1	31.8	−8.2	(85%,5 %,10%)	CB 1 opening	386
16	E	≈ 0	≈ 0	29	−8.6	(89%,0%,11%)	LLL Fault with CB1 opening (R_f = 0.5 Ω)	230
17	E	≈ 0	≈ 0	29	−8.6	(89%,0%,11%)	LLL Fault with CB1opening (R_f = 1 Ω)	237
18	E	≈ 0	≈ 0	29	−8.6	(89%,0%,11%)	LLL Fault with CB1 opening (R_f = 5 Ω)	240

* Voltage support: (E) Enabled, (D) Disabled; ΔP/ΔQ Computed active and reactive power imbalances; $\Delta P_{PCC}/\Delta Q_{PCC}$ Active and reactive power imbalances measured at the PCC; TT: Tripping time; Load composition: It represents the % of each type of load according to the voltage-dependence load modelling.

divided into two sub-sections. The first sub-section corresponds to the events that cause an islanding event (i.e., those which imply the operation of either CB_1 or CB_2). The second one has tested the non-islanding events (i.e., events which do not imply the CB opening but also cause voltage deviations).

4.3.1. Islanding events

The islanding events can be divided into two major groups. The first one considers a voltage-dependent composite load model. The second one is based on the procedure defined by the IEEE 929-2000 standard [37], which suggests a parallel RLC load with high power quality factors.

The results obtained in the first set of islanding events are summarized in Table 6. However, the most relevant events in terms of power imbalance are displayed in separate figures. Particularly, these events belong to the trained cases 1 to 8 (see the first column of Table 6) and are depicted in Figs. 7–10. A comparison between the results with (solid lines) and without (dashed lines) the voltage support mode is shown in these figures.

The plotted variables in these Figures are as follows; V_{PCC} (first plot), dV_{PCC}/dt (second plot), $d\delta/dt$ (third plot), active and reactive powers at PCC (fourth plot) and the tripping signal of the ID functionality (fifth plot). For all events, islanding begins at t = 1 s and ends when the CB reclosing takes place at 2.5 s. Each trained case belongs to a particular power imbalance scenario.

If the voltage support is enabled, a reactive power imbalance between the MG and the grid is introduced. Therefore, this reactive imbalance will be traduced into frequency oscillations [21]. On the contrary, if this support is disabled, both active and reactive power imbalances are negligible, precisely when the IO is more challenging to identify.

Cases 3 to 6 of Table 6 deserve a particular discussion. The imbalance values summarized in the third and fourth columns are computed according to the difference between the amount of generation and load, without considering the effect of the bidirectional charger. Meanwhile, the fifth and sixth columns are the actual power imbalance measured at the PCC, where the impact of the battery charger is considered. Essentially, the main difference between these values depends on two factors; the voltage support and the power-sharing strategy.

As stated earlier, if the voltage support mode is enabled, a reactive-power imbalance is introduced. Indeed, this reactive-power imbalance between the MG and the grid depends on the voltage at the PCC. On the contrary, if the SOC is above 90% or below 10 %, the MG will inject active power into the grid. Thence, an additional active-power imbalance will be observed at the PCC.

Since fuses generally protect LV feeders, the only events that can imply the complete circuit opening for the three phases are those originated by three-phase faults. Consequently, to assess the islanding events caused by faults at the LV feeder, only three-phase faults have been simulated; see trained cases 16 to 18 of Table 6.

The islanding events simulated according to the IEEE 929-2000 standard are summarized in Table 7. The zero-power mismatch case has been evaluated considering several quality factors (see cases 1 to 5 of Table 7). Furthermore, cases 6 and 7 of Table 7 have considered large power imbalances.

4.3.2. Non-islanding events

This sub-section is focused on testing those events where voltage drops and voltage angle oscillations occur, but the MG is not islanded. The simulated non-islanding events are summarised in Table 8. The eleven events listed in Table 8 can be divided into four major groups, as follows:

1. Faults upstream the feeder object of study (i.e., faults occurred at either the MV grid or at the neighbour LV) feeders (e.g., see the trained cases 1 to 6).
2. Induction motors starting. (Trained case 7).
3. Capacitor bank switching. (Trained case 8).
4. Sudden load connections (Trained cases 9 to 11)

Among all summarised non-islanding events in Table 8, a representative sample of them is shown in separate figures. The results of the trained cases 1, 2 and 4 of Table 8 are displayed in Fig. 11, where each column of that figure plots a particular type of fault (i.e., first column for case 1, second column for case 2 and the third column for case 4). The

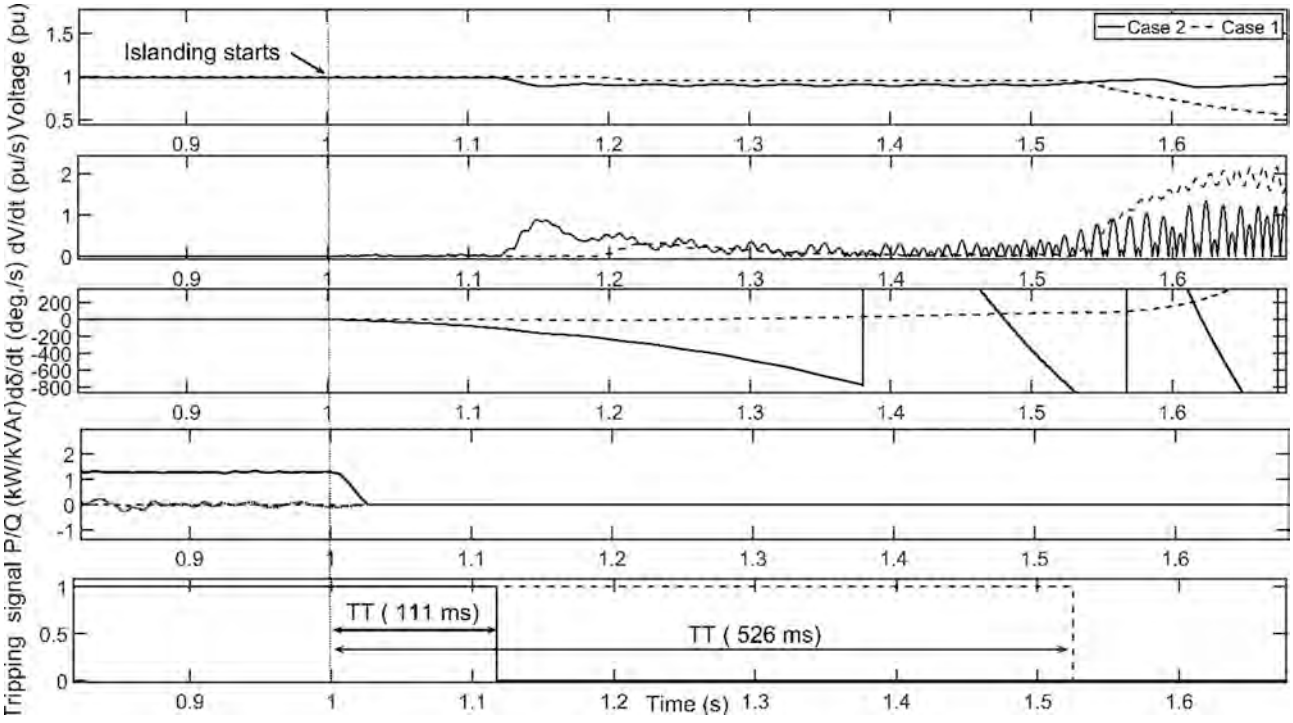

Fig. 7. Results obtained for the trained cases 1 and 2 of Table 6.

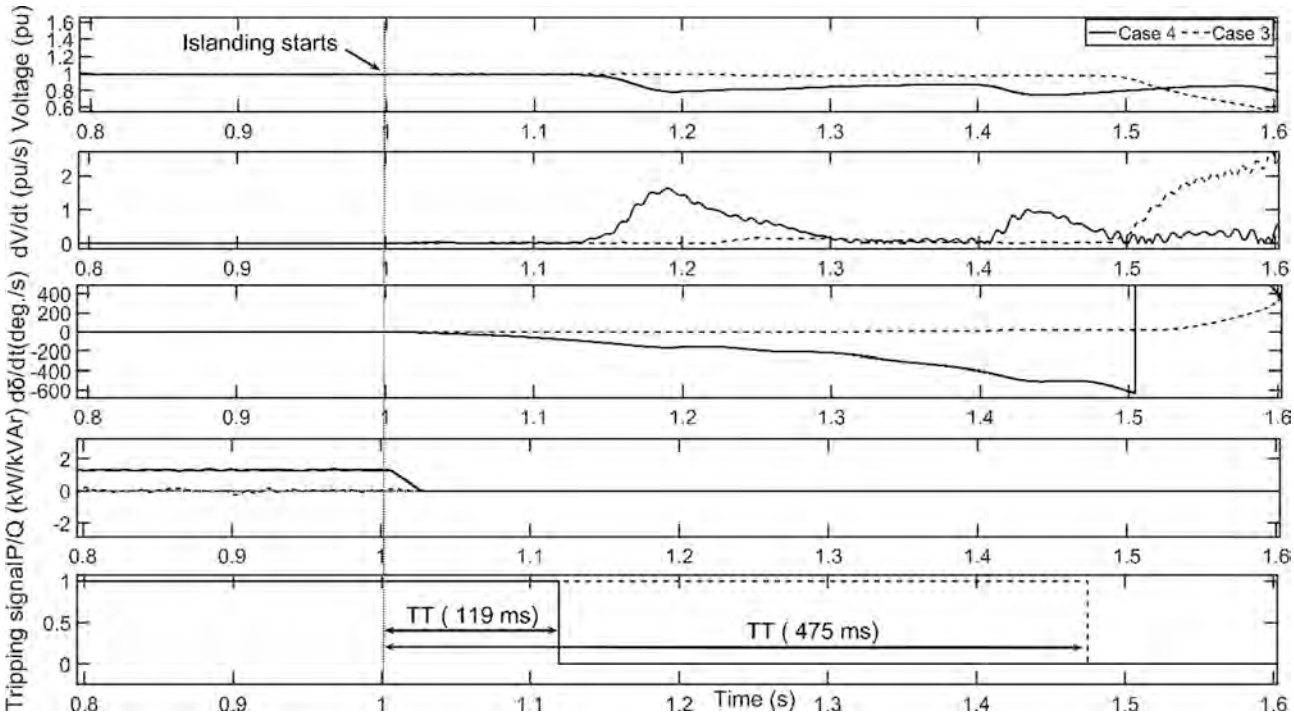

Fig. 8. Results obtained for the trained cases 3 and 4 of Table 6.

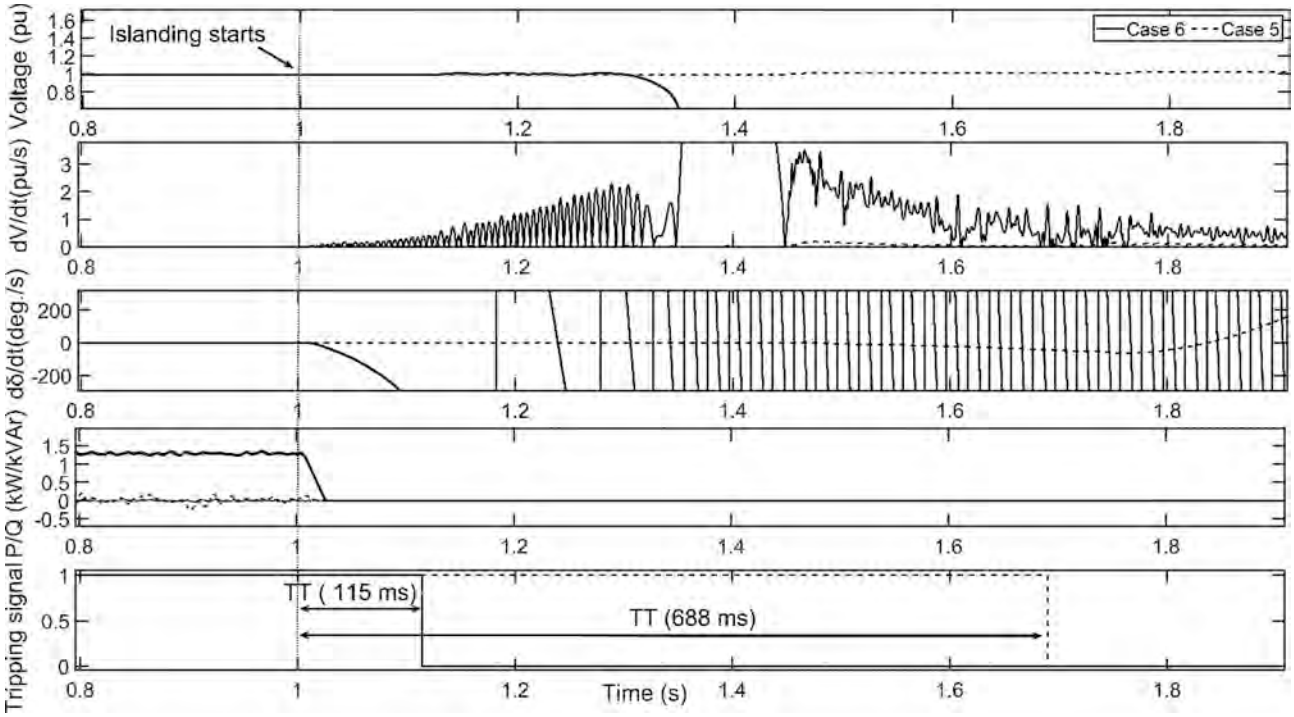

Fig. 9. Results obtained for the trained cases 5 and 6 of Table 6.

three voltage sags observed in Fig. 11 have been obtained by simulating faults at the primary winding of the MV/LV transformer TR_3 (see Fig. 1).

Case studies 7 and 8 of Table 8 have investigated the voltage oscillations caused by the induction motor starting and capacitor bank switching, respectively.

Eventually, the transient effects during a sudden load change in the MG are analyzed; see events 9 to 11 of Table 8. Besides, case 9 is displayed in Fig. 12, which has been obtained from case study 1 of Section 4 (see Fig. 6 at t = 40 s). By observing the five plots of Fig. 12, it can be drawn that although some variables slightly deviate during 200 ms, crucially, the DG is not tripped.

4.4. Selection of threshold settings for islanding detection

As seen in the previous subsection, the first stage of the MA becomes crucial to identify the occurrence of an islanding event and avoid false

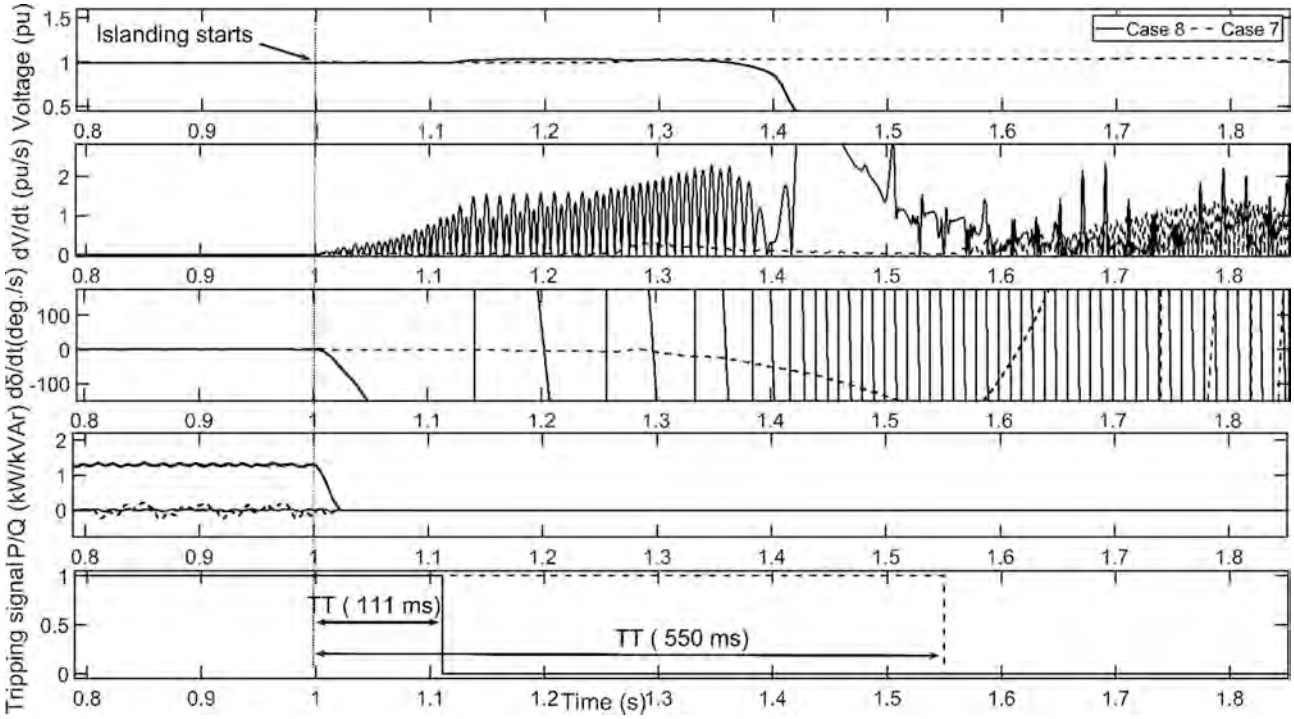

Fig. 10. Results obtained for the trained cases 7 and 8 of Table 6.

Table 7
Results with the IEEE 929-2000 test system.

Case no.	ΔP (%)	ΔQ (%)	Q_f	TT (ms)
1	0	0	2.5	597
2	0	0	2	344
3	0	0	1.5	492
4	0	0	1	409
5	0	0	0.5	369
6	−52	49	–	37
7	−50	−49	–	37

tripping operations during non-islanding events. By observing the results where the faults have been simulated, the dV_{PCC}/dt proved to be well above the 0.1 pu/s; see the second plot in each column of Fig. 11. Accordingly, the threshold for the ROCOV has been set to 0.1 pu/s.

The ROCOVPA used in this paper proved to be a reliable indicator for identifying islanding scenarios; see, for instance [33–34,36]. However, this derivative becomes non-zero during some non-islanding events. Indeed, the ID of the proposed MA has implemented very low thresholds to achieve zero-NDZ during islanding events, which implies a high risk of misidentification during non-islanding events. A particular case of interest among these non-islanding events is caused by the sudden load changes in the MG when the battery reference is modified. Nonetheless, by observing the results displayed in Fig. 12, the thresholds settings and time delays used for ID proved adequate.

4.5. Results discussion

The previous two subsections have shown the results of the simulations carried out with the proposed MA. Crucially, as has been demonstrated, the ID functionality correctly identifies both the islanding events with zero-power imbalances and the non-islanding events.

By observing the TTs in Table 6, it can be noticed that when the voltage support is enabled, the islanding condition is identified in around 100 ms (see trained cases 2,4,6 and 8). This fast detection time is due to the frequency oscillation resulting from the reactive-power mismatch, which causes frequency tripping (for both under and above). Conversely, once the voltage support is disabled, both active and reactive power imbalances measured at the PCC are negligible (see trained cases 1,3,5 and 7), and thereby, the obtained TTs are larger. The

Table 8
Non-Islanding Events description.

Trained cases	Event description	Fault Type*	Event location	FCT* (ms)	Duration (s)	Tripping Signal
1	Fault	SLG Fault ($R_f = 5\ \Omega$)	MV Bus	200	0.2	No Trip
2	Fault	LLG Fault ($R_f = 5\ \Omega$)	MV Bus	200	0.2	No Trip
3	Fault	LL Fault ($R_f = 5\ \Omega$)	MV Bus	200	0.2	No Trip
4	Fault	LLL Fault($R_f = 5\ \Omega$)	MV Bus	200	0.2	No Trip
5	Fault	LLL Fault ($R_f = 0\ \Omega$)	LV Feeder	100	0.1	No Trip
6	Fault	SLG Fault ($R_f = 10\ \Omega$)	LV Feeder	400	0.4	No Trip
7	IM starting 4 × 160 kW	–	LV Feeder	–	0.4	No Trip
8	Capacitor bank switching (150 kVAr)	–	LV Feeder	–	0.1	No Trip
9	Load Variation	–	MG	–	0.2	No Trip
10	Load Variation	–	MG	–	0.2	No Trip
11	Load Variation	–	MG	–	0.2	No Trip

* R_f: Resistance fault; Fault type (SLG = Single-line to ground Fault, LL = Line-to-line fault; LLL Fault = Three-phase Fault; LLG = Two-phase to ground Fault; LLLG: Three-phase to ground Fault); FCT: Fault clearing time.

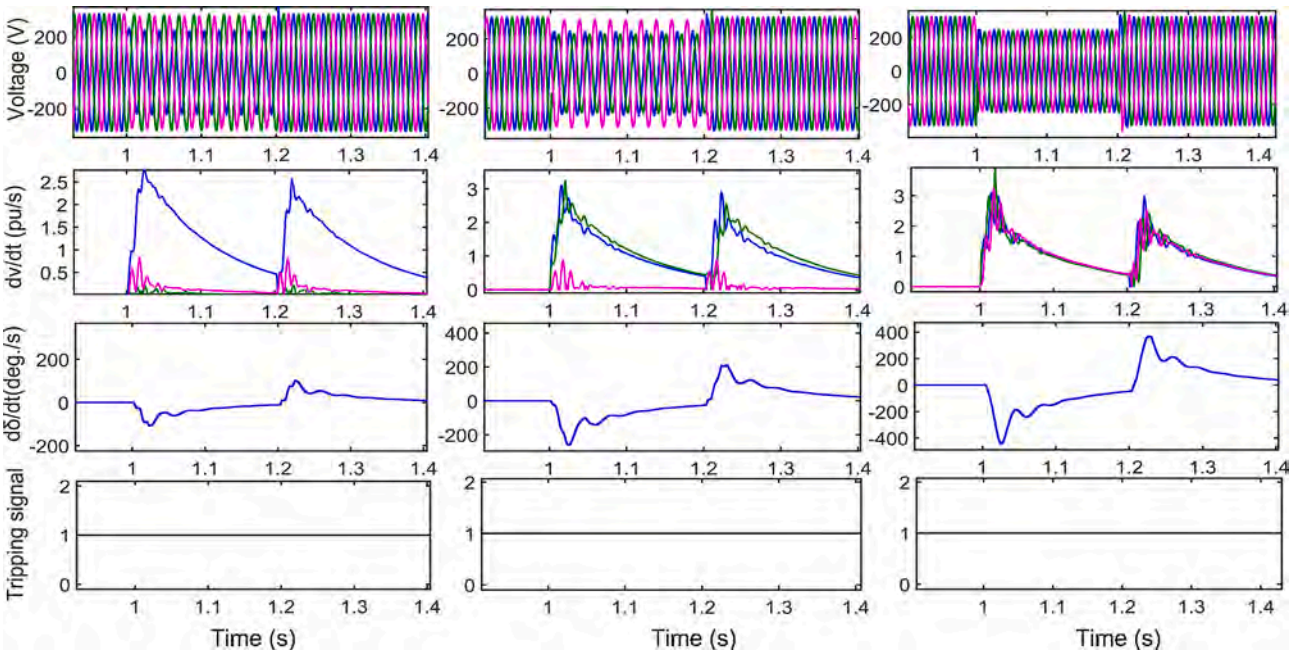

Fig. 11. Results of non-islanding events corresponding to trained cases 1, 2, and 4 of Table 7.

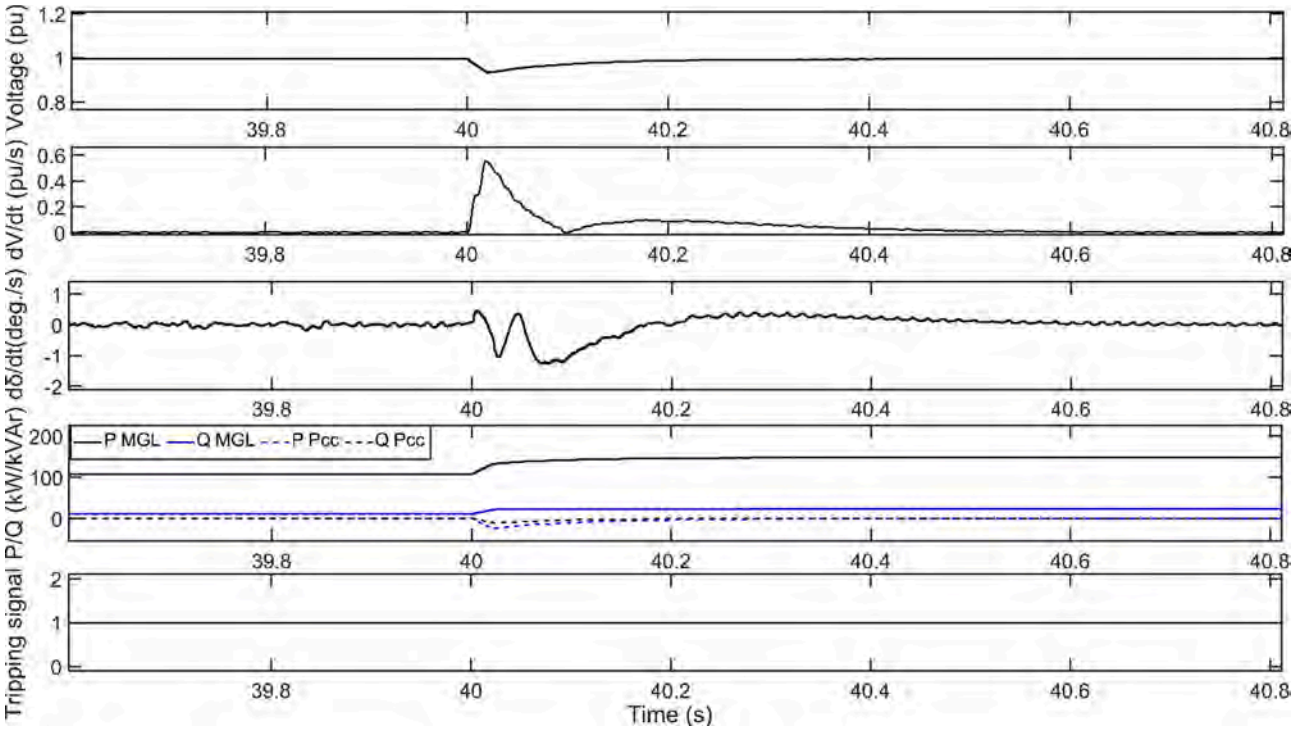

Fig. 12. Results obtained during a load change in the MG.

slight difference observed between these cases is the power delivered by the BESS and the load model composition for each case.

As stated in the previous section, if the absolute value of the mismatch between the PV generation and MGLs exceeds P_{TH}, the charger reference is set to P_{MIN}. On the contrary, the reference is set to $-P_{MAX}$. Thus, an initial low active power imbalance will become positive by modifying the BESS charger reference. However, in cases with large active power imbalances (either positive or negative), the initial imbalance remains unchanged after the VSC_2 reference change.

As is stated in [21,36], in DNs with inverter-based DGs, if the active power of the DG is larger than load, an over-voltage event takes place. By contrast, if the load power is larger than the DG power, an under-voltage will then occur. This effect is observed at t = 1.55 s in the first plot of Fig. 7, which belongs to case 1 of Table 6. However, regardless of the drop in the voltage amplitude, its angle also deviates from the established thresholds, making the algorithm correctly identify the IO.

On the other hand, cases 3, 5 and 7 of Table 6 have larger imbalances than P_{TH}. Therefore, when the reference of the VSC_2 is set to P_{MIN}, case 3 has a negative imbalance, whereas cases 5 and 7 have positive imbalances. This aspect can be observed in the first plot of Fig. 8, where at

t = 1.5 s, the voltage amplitude remarkably decreases due to the negative imbalance. By contrast, in Figs. 9 and 10, a slight increase in the voltage magnitude is observed after the change in the reference of the VSC_2.

From the results provided in Table 7, it has been demonstrated that all islanding events are detected by the proposed ID method if the test system recommended by the IEEE 929-2000 Std. is considered [37]. It is also observed that the higher the power quality factor, the higher the tripping time. As is suggested by this standard, islanding should be identified with less than ten cycles for islanding events with a power mismatch larger than 50 % with a power factor of more than 0.95. The latter casuistry has been considered in cases 6 and 7 of Table 7, where the method trips in 37 ms.

The active and reactive power imbalances of Table 6 are computed as follows

$$\Delta \mathrm{P}\,(\%) = \frac{P_{DG}\,(t_i) - P_{MGL}\,(t_i)}{P_{DG}\,(t_i)} \cdot 100 \tag{13}$$

$$\Delta Q\,(\%) = \frac{Q_{DG}\,(t_i) - Q_{MGL}\,(t_i)}{P_{DG}} \cdot 100 \tag{14}$$

$$\Delta \mathrm{P}_{PCC}(\%) = \frac{P_{PCC}(t_i)}{P_{DG}} \cdot 100 \tag{15}$$

$$\Delta Q_{PCC}(\%) = \frac{Q_{PCC}(t_i)}{P_{DG}} \cdot 100 \tag{16}$$

where ΔP and ΔQ are the computed active and reactive power imbalances both expressed as a percentage, whereas the ΔP_{PCC} and ΔQ_{PCC} belong to those imbalances measured at the PCC. The differences between the power imbalances in (13–14) and (15–16) are due to the voltage support and the BESS strategies' effects. The reactive-power imbalances of (14) and (16) are computed as a percentage of the DG active power (P_{DG}), which is used in some ID studies, see [19,20].

5. Comparison with other existing techniques

This article has proposed a MA that handles several functionalities all at once for a grid-connected MG. Therefore, the comparison between the proposed methodology and other techniques is made for each particular functionality separately (i.e., ID, voltage control and power sharing).

- The recently published articles about ID have significantly reduced the NDZ [39–42] but still have undetectable regions. Indeed, these articles have explored the ID with advanced techniques but have not considered other functionalities. In [26,27], the simultaneous combination of ID and LVRT capabilities has been investigated for grid-connected PV-based scenarios. Nevertheless, in [27], only scenarios with large power imbalances have been evaluated. Therefore, the NDZ zone of the ID cannot be compared. Moreover, it uses the frequency shifting technique as active-based ID, which continuously distorts the power quality of the grid [38,43]. On the other hand, even though the approach proposed in [26] has analyzed many scenarios, the zero-power imbalance case scenario has not been tested.
- Although the recently published articles towards the voltage control in DNs with DGs have considered innovative approaches with multi-agent algorithms, they have neither considered the power-sharing of a microgrid with BESSs nor the ID. For instance, see [5,12,25].
- Within the scope of energy management and power-sharing in MG applications, many articles have been published. Among them, several recent studies can be found in [3,4,6,8]. Particularly, the fully distributed multi-functional algorithm in [3] has achieved outstanding results for MGs control. Nonetheless, none of these articles have explored the ID.

Having said all that, the proposed MA has achieved a zero-NDZ in ID, which enhances the current status of some studies within this field. In addition to the ID capability, the MA also provides voltage support to the distribution grid whilst managing the power sharing of the MG.

6. Conclusion

The current paper has proposed an algorithm for a GCMG formed by a PV-based DG unit and a BESS, which simultaneously addresses the power sharing, voltage support and ID issues. The assessment of the proposed approach has been divided into two major groups of simulations. The first is an optimization process focused on testing the MA capabilities such as power-sharing and voltage support for a 24-hour framework. The second, aimed at identifying the IOs, have tested a set of scenarios considering both islanding and non-islanding events.

In light of the obtained results in Section 4, it has been demonstrated that the algorithm reduces the peak power of the MG while providing voltage support to the grid. Furthermore, if any islanding condition is suspected during the optimization process, a hybrid ID method is initiated.

The first part of the ID functionality is based on local measurements and considers very low threshold settings. Meanwhile, the active-based part takes advantage of the BESS bidirectional charger as a valuable tool for identifying the islanding condition. The dependability of the ID function has been evaluated for a large set of scenarios considering both islanding and non-islanding events. The islanding events have been simulated in two different scenarios. The first one considers a voltage-dependent composite load model, and the second belongs to the reduced test system recommended by the IEEE 929-2000 Std. Concerning the particular case of non-islanding events, a particular interesting non-islanding event is the one that occurs during a sudden change in the MG load. It is worth pointing out that selecting the optimal thresholds is a bottleneck in most ID studies, which has been successfully fulfilled in this MA for both islanding and non-islanding events.

A remarkable aspect of this method is that additional devices or signal injections are not required, unlike some other active-based ID techniques. Therefore, the cost of the installation is reduced, and power quality degradation is avoided. Additionally, the tripping time of all tested events is far below the maximum time of 2 s established by the IEEE Std. 1647-2018.

Finally, in order to highlight the novelty of the presented method, a comparison with the recently published articles has been carried out. Thus, by observing the comparison in Section 5, there is ample evidence of the high profits provided by this method in terms of reliability, practicality and effectiveness.

CRediT authorship contribution statement

Alexandre Serrano-Fontova: Methodology, Software, Conceptualization, Investigation, Writing – original draft. **Mohamed Azab:** Conceptualization.

Declaration of Competing Interest

The authors declare that they have no known competing financial interests or personal relationships that could have appeared to influence the work reported in this paper.

References

[1] Olivares DE, Mehrizi-Sani A, Etemadi AH, Canizares CA, Iravani R, Kazerani M, et al. Trends in microgrid control. IEEE Trans Smart Grid 2014;5(4):1905–19. https://doi.org/10.1109/TSG.2013.2295514.

[2] Jiang Q, Xue M, Geng G. Energy management of microgrid in grid-connected and stand-alone modes. IEEE Trans Power Syst 2013;28(3):3380–9. https://doi.org/10.1109/TPWRS.2013.2244104.

[3] Shafiee Q, Nasirian V, Vasquez JC, Guerrero JM, Davoudi A. A multi-functional fully distributed control framework for AC microgrids. IEEE Trans Smart Grid 2018;9(4):3247–58. https://doi.org/10.1109/TSG.2016.2628785.
[4] Brandao DI, Ferreira WM, Alonso AMS, Tedeschi E, Marafao FP. Optimal multiobjective control of low-voltage AC microgrids: Power flow regulation and compensation of reactive power and unbalance. IEEE Trans Smart Grid 2020;11(2):1239–52. https://doi.org/10.1109/TSG.516541110.1109/TSG.2019.2933790.
[5] Mahmoud K, Mahmoud M, Hussein M-N, Lehtonen M. Optimal voltage control in distribution systems with intermittent PV using multi-objective Grey-Wolf-Lévy. IEEE Systems 2020. https://doi.org/10.1109/JSYST.2019.2931829.
[6] William MF, Menehgini IR, Brandao DI, Guimaraes FG. Preference cone based multi-objective evolutionary algorithm applied to optimal management of distributed energy resources in microgrids. Appl Energy 2015;6(1):158–65. https://doi.org/10.1016/j.apenergy.2020.115326.
[7] Alahakoon D, Yu X. Smart electricity meter data intelligence for future energy systems: A survey. IEEE Trans Ind Informatics 2016;12(1):425–36. https://doi.org/10.1109/TII.2015.2414355.
[8] Schram WL, Lampropoulos I, van Sark WGJHM. Photovoltaic systems coupled with batteries that are optimally sized for household self-consumption: Assessment of peak shaving potential. Appl Energy 2018;223:69–81. https://doi.org/10.1016/j.apenergy.2018.04.023.
[9] Ahmadian A, Sedghi M, Mohammadi-ivatloo B, Elkamel A, Aliakbar Golkar M, Fowler M. Cost-benefit analysis of V2G implementation in distribution networks considering PEVs battery degradation. IEEE Trans Sustain Energy 2018;9(2):961–70. https://doi.org/10.1109/TSTE.2017.2768437.
[10] Guerra G, Martinez-Velasco JA. Optimum allocation of distributed generation in multi-feeder systems using long term evaluation and assuming voltage-dependent loads. Sustain Energy, Grids Networks 2016;5:13–26. https://doi.org/10.1016/j.segan.2015.10.005.
[11] Martinez JA, Guerra G. A parallel monte carlo method for optimum allocation of distributed generation. IEEE Trans Power Syst 2014;29(6):2926–33. https://doi.org/10.1109/TPWRS.2014.2317285.
[12] Bedawy A, Yorino N, Mahmoud K, Zoka Y, Sasaki Y. Optimal voltage control strategy for voltage regulators in active unbalanced distribution systems using multi-agents. IEEE Trans Power Syst 2020;35(2):1023–35. https://doi.org/10.1109/TPWRS.5910.1109/TPWRS.2019.2942583.
[13] Taul MG, Wu C, Chou S-F, Blaabjerg F. Optimal controller design for transient stability enhancement of grid-following converters under weak-grid conditions. IEEE Trans Power Electr 2021;36(9):10251–10264. https://doi.org/10.1109/TPEL.2021.3066205.
[14] Hasanien HM. An adaptive control strategy for low voltage ride through capability enhancement of grid-connected photovoltaic power plants. IEEE Trans Power Syst 2015;31(4):3230–7. https://doi.org/10.1109/TPWRS.2015.2466618.
[15] Eftekharnejad S, Vittal V, Heydt GT, Keel B, Loehr J. Impact of increased penetration of photovoltaic generation on power systems. IEEE Trans Power Syst 2013;28(2):893–901. https://doi.org/10.1109/TPWRS.2012.2216294.
[16] Cherrington R, Goodship V, Longfield A, Kirwan K. The feed-in tariff in the UK: A case study focused on domestic photovoltaic systems. Renew Energy 2013. https://doi.org/10.1016/j.renene.2012.06.055.
[17] Eftekharnejad S, Heydt GT, Vittal V. Optimal generation dispatch with high penetration of photovoltaic generation. IEEE Trans Sustain Energy 2015;6(3):1013–20. https://doi.org/10.1109/TSTE.2014.2327122.
[18] Alexandre S-F, Juan AM, Pau C-T, Ricard B. A robust islanding detection method with zero-non-detection zone for distribution systems with DG. Int J Electr Power Energy Syst 2021;133:107247. https://doi.org/10.1016/j.ijepes.2021.107247.
[19] Paiva SC, Ribeiro RLdA, Alves DK, Costa FB, Rocha TdOA. A wavelet-based hybrid islanding detection system applied for distributed generators interconnected to AC microgrids. Int J Electr Power Energy Syst 2020;121:106032. https://doi.org/10.1016/j.ijepes.2020.106032.
[20] Xie X, Huang C, Li D. A new passive islanding detection approach considering the dynamic behavior of load in microgrid. Int J Electr Power Energy Syst 2020;117:105619. https://doi.org/10.1016/j.ijepes.2019.105619.
[21] Cui Q, El-Arroudi K, Joos G. Islanding detection of hybrid distributed generation under reduced nondetection zone. IEEE Trans Smart Grid 2018;9(5):5027–37. https://doi.org/10.1109/TSG.516541110.1109/TSG.2017.2679101.
[22] Serrano-Fontova A, Casals-Torrens P, Bosch R. Power quality disturbances assessment during unintentional islanding scenarios. A contribution to voltage sag studies. Energies 2019;12(16):3198. https://doi.org/10.3390/EN12163198.
[23] IEEE Standards Coordinating Committee 21. IEEE Application Guide for IEEE Std 1547TM, IEEE Standard for Interconnecting Distributed Resources with Electric Power Systems; 2018.
[24] Kim M-S, Haider R, Cho G-J, Kim C-H, Won C-Y, Chai J-S. Comprehensive review of islanding detection methods for distributed generation systems. Energies 2019;12(5):837. https://doi.org/10.3390/en12050837.
[25] Zhang C, Xu Y. Hierarchically-Coordinated Voltage/VAR control of distribution networks using PV inverters. IEEE Trans Smart Grid 2020;11(4):2942–53. https://doi.org/10.1109/TSG.516541110.1109/TSG.2020.2968394.
[26] Das PP, Chattopadhyay S. A voltage-independent islanding detection method and low-voltage ride through of a two-stage PV inverter. IEEE Trans Ind Appl 2018;54(3):2773–83. https://doi.org/10.1109/TIA.2017.2788433.
[27] Dietmannsberger M, Grumm F, Schulz D. Simultaneous Implementation of LVRT Capability and anti-islanding detection in three-phase inverters connected to low-voltage grids. IEEE Trans Energy Convers 2017;32(2):505–15. https://doi.org/10.1109/TEC.2017.2662059.
[28] Laaksonen H, Hovila P, Kauhaniemi K. Combined islanding detection scheme utilizing active network management for future resilient distribution networks. IET J Eng 2018;2018(15):1054–60. https://doi.org/10.1049/joe.2018.0202.
[29] The Mathworks Inc. MATLAB-2016-MathWorks. www.mathworks.com/products/matlab; 2016.
[30] Restrepo Mauricio, Morris Jordan, Kazerani Mehrdad, Canizares Claudio A. Modeling and testing of a bidirectional smart charger for distribution system EV integration. IEEE Trans Smart Grid 2018;9(1):152–62. https://doi.org/10.1109/TSG.2016.2547178.
[31] Ovalle A, Ramos G, Bacha S, Hably A, Rumeau A. Decentralized control of voltage source converters in microgrids based on the application of instantaneous power theory. IEEE Trans Ind Electron 2014;62(2):1152–62. https://doi.org/10.1109/TIE.2014.2336638.
[32] Yazdani Amirnaser, Iravani Reza, editors. Voltage-Sourced Converters in Power Systems. Hoboken, NJ, USA: John Wiley & Sons, Inc.; 2010.
[33] Samui A, Samantaray SR. Assessment of ROCPAD relay for islanding detection of distributed generation. IEEE Trans Smart Grid 2011. https://doi.org/10.1109/TSG.2011.2125804.
[34] Samet H, Hashemi F, Ghanbari T. Islanding detection method for inverter-based distributed generation with negligible nondetection zone using energy rate of rate of change of phase voltage. IET Gener Transm Distrib 2015. https://doi.org/10.1049/iet-gtd.2015.0638.
[35] Ali Abdelfatah, Mahmoud Karar, Lehtonen Matti. Multi-objective photovoltaic sizing with diverse inverter control schemes in distribution systems hosting EVs. IEEE Trans Ind Inform 2021;17(9):5982–92. https://doi.org/10.1109/TII.942410.1109/TII.2020.3039246.
[36] Seyedi M, Taher Seyyed A, Ganji B, Guerrero Josep M. A hybrid islanding detection technique for inverter-based distributed generation. Int Trans Electr Energ Syst 2019. https://doi.org/10.1002/2050-7038.12113.
[37] IEEE recommended practice for utility interface of photovoltaic (pv) systems. IEEE Std. 929-2000. http://dx.doi.10.1109/IEEESTD. 2000.91304.
[38] Gupta Pankaj, Bhatia RS, Jain DK. Average absolute frequency deviation value based active islanding detection technique. Int Trans Electr Energ Syst 2015;6(1):26–35. https://doi.org/10.1109/TSG.2014.2337751.
[39] Bakhshi-Jafarabadi Reza, Sadeh Javad, Popov Marjan. Maximum power point tracking injection method for islanding detection of grid-connected photovoltaic systems in microgrid. IEEE Trans Power Deliv 2021;36(1):168–79. https://doi.org/10.1109/TPWRD.6110.1109/TPWRD.2020.2976739.
[40] Kim MS, Haider R, Cho GJ, Kim CH, Won CY, Chai JS. An Islanding detection technique for inverter-based distributed generation in microgrids comprehensive review of islanding detection methods for distributed generation systems. Energies 2020. https://doi.org/10.3390/en14010130.
[41] Xie X, Xu W, Huang C, Fan X. New islanding detection method with adaptively threshold for microgrid. Electr Power Syst Res 2021;195:58–66. https://doi.org/10.1016/j.epsr.2021.107167.
[42] Bakhshi-Jafarabadi Reza, Sadeh Javad, Chavez Jose de Jesus, Popov Marjan. Two-level islanding detection method for grid-connected photovoltaic system-based microgrid with small nondetection zone. IEEE Trans Smart Grid 2021;12(2):1063–72. https://doi.org/10.1109/TSG.516541110.1109/TSG.2020.3035126.
[43] Liu F, Zhang Y, Xue M, Lin X, Kang Y. Investigation and evaluation of active frequency drifting methods in multiple grid-connected inverters. IET Power Electron Apr. 2012;5(4):485–92.